Topological acoustics with orbital-dependent gauge fields

Feng Gao, Yu-Gui Peng,* Qi-Li Sun, Xiao Xiang, Chen Zheng, and Xue-Feng Zhu†
School of Physics and Innovation Institute, Huazhong University of Science and Technology, Wuhan 430074, China

(Received 4 September 2023; revised 27 November 2023; accepted 11 December 2023; published 20 December 2023; corrected 5 March 2024)

The synthetic gauge field, projectively enriching the algebraic structure of spatial symmetries, has become a hotspot in topological physics recently. The intrinsic orbital degrees of freedom, playing a fundamental role in solid-state materials and offering an alternative platform, have not yet been studied extensively in classical wave systems, such as acoustic systems. Here we propose orbital-dependent gauge fields by utilizing the intrinsic degenerate p orbitals in a square lattice of coupled acoustic cavities. To realize the orbital-related synthetic gauge fields, an acoustic disk-shaped resonator hosting degenerate p orbitals is designed, where the signs of transverse and longitudinal hoppings can be simultaneously tailored on demand by tuning the geometries of coupling waveguides in the dimer units. We then show two different types of orbital-dependent topological insulators resting with the orbital-dependent gauge fields via the tight-binding method and full-wave simulation. Moreover, an orbital-dependent semimetal phase is revealed in the square lattice with a varied dimerization pattern. Our findings reveal the existence of abundant physical phenomena as the cavity orbitals and gauge fields meet with the topology, initializing the framework for orbital-related topological physics and opening up opportunities for potential multifunctional acoustic applications, such as sound sensing and trapping.

DOI: 10.1103/PhysRevApplied.20.064036

I. INTRODUCTION

Synthetic gauge fields (SGFs) possess the characteristics to make neutral particles act as if they go through an external field, which also play a crucial role in wave physics. In previous works, the SGFs were generated by virtue of some external modulations [1,2] or judicious geometry design [3,4]. Plenty of fascinating effects and related applications have been realized by utilizing SGFs, such as the anomalous light guiding [5,6], negative wave refraction [7], spectrum controls [8] and dispersionless engineering [9]. SGFs were also proposed and reported in the synthetic dimensions [10,11]. Nonetheless, SGFs provide an avenue for realizing topological insulators (TIs) in photonics [12] and acoustics [13]. For instance, the topologically protected one-way photonic edge states were generated by a gauge potential induced via the phase modulation [12], and an acoustic Floquet TI was illustrated by SGFs based on a slow on-site rotating modulation scheme [13]. As π gauge flux exists per each plaquette, the acoustic quadrupole TIs [14,15] and the photonic Aharonov-Bohm effect can thus be realized [16,17].

Recently, SGFs have been discovered to play a role in topological band physics at a more fundamental level, which alter the algebraic structure of space-group symmetries and enable the inherent projective representation [18–22]. For instance, in the absence of SGFs, two primitive translation symmetries in the rectangular lattice are supposed to commute with each other, while they alter to be noncommutative with the π flux induced by SGFs. By means of the projective symmetry algebra, a plethora of alternative topological phases and insulators have been illustrated, such as the Brillouin-Klein bottle insulators [23], Möbius insulators [24], as well as the spinless Kramers-Majorana modes [20].

The intrinsic orbitals, which play a role in correlated electronic systems [25] and solid-state materials [26], have yielded plenty of peculiar topological phases involving the orbital superfluidity [27] and topological semimetals [28]. More recently, related researches on orbitals have been expanded to the realms of photonics [29,30] and electronics [31,32]. For instance, the optically induced magnetic topological edge states were visualized in the zigzag-chain of dielectric resonant structures [29]. Besides, lasing via a topologically protected edge mode has been illustrated in a one-dimensional zigzag lattice [30]. The p-orbital band manipulations and Dirac cones were also realized in the electronic Lieb lattice [31] and honeycomb lattice [32] via the scanning tunneling microscopes, respectively. Recently, a unique type of photonic quadrupole topological insulator was reported by leveraging both s and

*ygpeng@hust.edu.cn
†xfzhu@hust.edu.cn

p orbital-type modes to generate the synthetic magnetic flux threading the lattice [33], and this mechanism was furtherly employed to illustrate the Möbius topological insulators and the Weyl-like semimetals [34,35]. Though the orbital degrees of freedom were witnessed to offer a powerful avenue in exploring the topological physics in various realms. Utilizing the intrinsic degenerate orbitals to design orbital-dependent SGFs as well as hybrid band topologies are left uncharted in acoustic systems.

In this work, we propose a composite acoustic square lattice supporting degenerate p orbitals, giving rise to the hybridization of a two-dimensional (2D) Su-Schrieffer-Heeger (SSH) lattice with zero flux per plaquette and a Möbius TI with synthetic π flux per plaquette. Resting with the tight-binding model (TBM), we systematically derive the Hamiltonians involving the orbital interactions among different lattice sites. To realize the orbital-dependent gauge fields in acoustic systems, we design on-site disk-shaped acoustic cavities hosting degenerate p orbitals and form the effective orbital-coupling mechanism, where the coupling signs can be tailored by the connection styles of linking waveguides in a dimer unit. Then we analyze the characteristics of energy bands in the model with/without applying coupling dimerization by TBM and full-wave simulation (FWS), which are in good agreement. By harnessing a strip supercell model, two types of hybrid orbital edge states are directly visualized. We thus confirm the orbital-dependent Möbius TI by the frequency responses and excitation field distributions in simulations. Furthermore, the orbital-dependent semimetal phase and flat-band feature in the square lattice are shown by an alternative dimerization coupling pattern. Our work provides a fundamental understanding of the interplay between acoustic orbital modes and synthetic gauge fields, shedding light on orbital-related topological physics and programmable acoustic devices.

II. ORBITAL-DEPENDENT GAUGE FIELD

We start with the schematics for two individual square lattices whose sites host different orbitals as displayed in Figs. 1(a) and 1(b). Clearly, the coupling patterns per plaquette of them are discriminative. Specifically, each site in Fig. 1(a) is equipped with p_x orbital. A dimerization of σ-type coupling between the adjacent sites exists in the x direction, as denoted by the dashed blue lines (negative coupling) with the couplings $t_{2\sigma} < t_{1\sigma} < 0$. Identical π-type coupling $t_{1\pi}$ exists in the y direction, as denoted by the solid black lines with $t_{1\pi} > 0$. The consequent synthetic flux is zero. In contrast, p_y orbital occupies each site in Fig. 1(b) and there exist the dimerization of π-type couplings with reversed signs marked by the dashed (solid) black lines denoting negative (positive) couplings in x direction and the same σ-type couplings $t_{1\sigma}$ in y direction, giving rise to a π flux per plaquette. On the basis of this feature, a composite square lattice comprising both the information in the lattices of Figs. 1(a) and 1(b) can be constructed, showing the orbital-dependent property. The Hamiltonian for the constructed composite square lattice based on the TBM reads as

$$\begin{aligned} H = -\sum \Big[& t_{1\sigma}\left(d^{\dagger}_{l,1}b_{l,1} + c^{\dagger}_{l,1}a_{l,1} + b^{\dagger}_{l,2}a_{l,2} + d^{\dagger}_{l,2}c_{l,2}\right. \\ & \left. + b^{\dagger}_{l-e_2,2}a_{l,2} + d^{\dagger}_{l-e_2,2}c_{l,2}\right) + t_{2\sigma}\left(d^{\dagger}_{l-e_1,1}b_{l,1} + c^{\dagger}_{l-e_1,1}a_{l,1}\right) \\ & + t_{1\pi}\left(\tilde{d}^{\dagger}_{l,1}\tilde{b}_{l,1} - \tilde{c}^{\dagger}_{l,1}\tilde{a}_{l,1} + \tilde{b}^{\dagger}_{l,2}\tilde{a}_{l,2} + \tilde{d}^{\dagger}_{l,2}\tilde{c}_{l,2} + \tilde{b}^{\dagger}_{l-e_2,2}\tilde{a}_{l,2}\right. \\ & \left. + \tilde{d}^{\dagger}_{l-e_2,2}\tilde{c}_{l,2}\right) + t_{2\pi}\left(\tilde{d}^{\dagger}_{l-e_1,1}\tilde{b}_{l,1} - \tilde{c}^{\dagger}_{l-e_1,1}\tilde{a}_{l,1}\right)\Big] + H.c., \end{aligned} \tag{1}$$

in which $a_l(\tilde{a}_l)$, $b_l(\tilde{b}_l)$, $c_l(\tilde{c}_l)$, and $d_l(\tilde{d}_l)$ stand for the σ-type (π-type) annihilation operators at four sites A, B, C, and D within a primitive cell as shown in Fig. 1(a), respectively, with the site position at l. The subscript i in $a_{l,i}$ denotes the projection direction along the primitive lattice vectors e_i ($i = 1, 2$). $t_{1\sigma}(t_{2\sigma})$ and $t_{1\pi}(t_{2\pi})$ correspond to the intracell (intercell) σ-type and π-type hopping amplitudes in x direction, respectively, while the hopping amplitudes for intra- and intercell are equal in y direction. As the Fourier transformation is used for all real-space operators and the eight-component spinors are considered, we derive the Hamiltonian in the momentum space

$$H(\mathbf{k}) = -\begin{pmatrix} 0 & D_1 & D_2 & 0 \\ D_1^{\dagger} & 0 & 0 & D_3 \\ D_2^{\dagger} & 0 & 0 & D_1 \\ 0 & D_3^{\dagger} & D_1^{\dagger} & 0 \end{pmatrix}, \tag{2}$$

in which the ingredients of D_i ($i = 1, 2, 3$) are

$$\begin{cases} D_1(\mathbf{k}) = e_2 e_2^{\dagger}\left(t_{1\sigma} + t_{1\sigma}e^{-i\mathbf{k}\cdot\boldsymbol{e_2}}\right) + o_2 o_2^{\dagger}\left(t_{1\pi} + t_{1\pi}e^{-i\mathbf{k}\cdot\boldsymbol{e_2}}\right) \\ D_2(\mathbf{k}) = e_1 e_1^{\dagger}\left(t_{1\sigma} + t_{2\sigma}e^{-i\mathbf{k}\cdot\boldsymbol{e_1}}\right) - o_1 o_1^{\dagger}\left(t_{1\pi} + t_{2\pi}e^{-i\mathbf{k}\cdot\boldsymbol{e_1}}\right) \\ D_3(\mathbf{k}) = e_1 e_1^{\dagger}\left(t_{1\sigma} + t_{2\sigma}e^{-i\mathbf{k}\cdot\boldsymbol{e_1}}\right) + o_1 o_1^{\dagger}\left(t_{1\pi} + t_{2\pi}e^{-i\mathbf{k}\cdot\boldsymbol{e_1}}\right) \end{cases}, \tag{3}$$

with $k=(k_x, k_y)$. In Eq. (2) e_i and o_i are the unit vectors orthogonal to each other ($t_{2\sigma} < t_{1\sigma} < 0$, $0 < t_{1\pi} < t_{2\pi}$). The equivalent Hamiltonian formed by the ingredient of p_y orbital in the lattice that carries π flux per plaquette can be expressed as

$$H_1 = t_{1\sigma}(1+\cos k_y)\Gamma_1 + t_{1\sigma}\sin k_y \Gamma_2 - (t_{1\pi} + t_{2\pi}\cos k_x)\Gamma_3 - t_{2\pi}\sin k_x \Gamma_4, \quad (3)$$

where $\Gamma_1 = \sigma_0 \otimes \tau_1$, $\Gamma_2 = \sigma_0 \otimes \tau_2$, $\Gamma_3 = \sigma_1 \otimes \tau_3$, $\Gamma_4 = \sigma_2 \otimes \tau_3$. σ_i and τ_i represent the Pauli matrices acting on the x and y sublattices, respectively. As the π flux exists, Eq. (3) does not respect the primitive translation symmetry $L_y = \sigma_0 \otimes \begin{pmatrix} 0 & 1 \\ e^{ik_y} & 0 \end{pmatrix}$. By employing a gauge transformation $G = \sigma_3 \otimes \tau_0$ to L_y, we can obtain the projective translation $\mathcal{L}_y = GL_y$ and $[\mathcal{L}_y, H_1] = 0$. Besides, the system also respects the chiral symmetry $\mathcal{S} = \sigma_3 \otimes \tau_3$. The effective Hamiltonian formed by the ingredient of p_x orbital can thus be acquired as

$$H_2 = t_{1\pi}(1+\cos k_y)\Gamma_1 + t_{1\pi}\sin k_y \Gamma_2 + (t_{1\sigma} + t_{2\sigma}\cos k_x)\Gamma_5 + t_{2\sigma}\sin k_x \Gamma_6, \quad (4)$$

where $\Gamma_5 = \sigma_1 \otimes \tau_0$, and $\Gamma_6 = \sigma_2 \otimes \tau_0$. Figure 1(c) shows the corresponding acoustic models for two types of dimer units. On the left of Fig. 1(c), the black dots in the sketch represent the sites hosting both p_x and p_y orbitals. The solid aqua line indicates the composite couplings for p orbitals, where the coupling signs are negative for σ-type hopping and positive for π-type hopping. To realize these demanding properties in the acoustic model, the disk-shaped resonators allowing for orthogonal degenerate p orbitals are designed, and a V-style waveguide linking the resonators, as shown in the subfigure next to the sketch, satisfies the reverse-sign coupling for the two orbitals in the dimer unit. Similarly, the sketch and acoustic model for the dimer unit with X-style negative couplings for both σ-type and π-type hopping are shown at the right panel of Fig. 1(c). To elucidate the coupling process and interaction mechanism, we choose the dimer unit cell with V-style coupling waveguides as an example to simulate its four eigenmodes, viz., the σ bonding, π bonding, π antibonding, and σ antibonding, respectively, with increasing frequencies, as displayed in Fig. 1(d). Here, the σ-type and π-type bondings correspond to two different types of coupling. Specifically, σ bonding describes the coupling between the cavity sites with orbital orientation parallel to the bonding direction, while π bonding describes the hopping for orbital orientation perpendicular to the bonding direction. By analyzing the frequencies of eigenmodes, we can find that the couplings for σ-type bonding and π-type bonding are negative and positive, respectively. A similar process can be operated to the dimer unit with X-style coupling linkages, where the couplings for σ-type bonding and π-type bonding are both negative and have the same value.

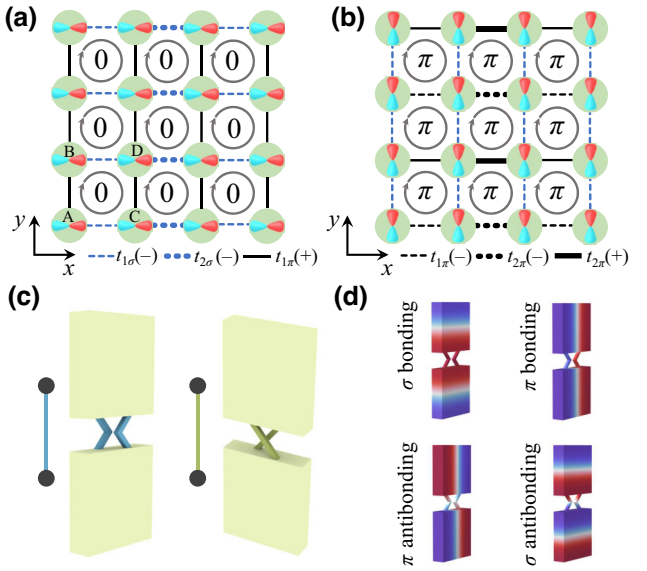

FIG. 1. Orbital-dependent square lattices without or with synthetic π flux per plaquette. (a),(b) Tight-binding lattices for orthogonal degenerate p orbitals with different synthetic fluxes. The lattice in (a) denotes a 2D SSH model with synthetic zero flux per plaquette by p_x orbital, and the one in (b) shows the Möbius TI with synthetic π flux per plaquette by p_y orbital. The dashed (solid) lines denote the negative (positive) hoppings. The blue (black) color represents the type of σ (π) hopping. The thinness and thickness of lines indicate the amplitudes of couplings. (c) The schematic acoustic models for hopping tunability in the dimer unit. Left: the aqua line denotes the reversed signs for transverse hopping (π, positive) and longitudinal hopping (σ, negative). The realizable acoustic model is constructed by two disk-shaped cavities connected by the V-style waveguides. Right: the olive line denotes the same sign (negative) for two types of hoppings. The acoustic model is constructed by two disk-shaped cavities connected by the X-style waveguides. (d) The eigenfields for the model with the V-style waveguide couplings.

Based on the degenerate p orbitals and coupling manners in the dimer cavities, the orbital-dependent gauge field for sound can be realized on demand in the designed square lattice, which can simultaneously have the characteristics of lattices in Figs. 1(a) and 1(b) via different orbital excitations. Therefore, we can realize a hybrid 2D SSH model with zero flux and the Möbius TI with synthetic π flux per plaquette in the same model.

III. ACOUSTIC IMPLEMENTATION

Here, we show the construction of realizable primitive cell model and discuss the band structures calculated by the TBM and FWS. Figure 2(a) displays a square-lattice model whose coupling strengths are the same ($|t_1| = |t_2|$). The disk-shaped square resonator with rigid walls is filled

with air, with the thickness $h = 10$ mm and side length $d = 40$ mm. As shown in Fig. 2(a), the widths of V-style and X-style coupling waveguides are, respectively, $d_1 = 2.23$ mm and $d_2 = 2.18$ mm, and the involving angle is $\theta_1 = 43°$. The lattice constant is $a = 106$ mm. In our case, the coupling strength can be engineered by manipulating the widths and angles of linking waveguides. Note that there exists a hidden hopping condition between degenerate p orbitals, viz., $t_{1\pi}/t_{2\pi} = t_{1\sigma}/t_{2\sigma}$, which must be satisfied when we design the V-style and X-style coupling waveguides. The band structures are shown in Fig. 2(b). Obviously, the band structures obtained by the TBM (solid line) match well with the ones simulated by the finite-element solver (circles). To be specific, the bulk bands corresponding to the p_y-orbital modes, as marked by the blue circles, are twofold degenerate over the entire Brillouin zone, where a fourfold Dirac point emerges as the result of the formation of π flux. The remaining orange-circle bands are the product of p_x-orbital modes. Since a coupling dimerization is introduced to the square lattice in x direction, as shown in Fig. 2(c), the band structures are changed with the degeneracy point lifted with an opened band gap, as shown in Fig. 2(d). In our calculation, the widths and involving angles of V-style and X-style intercell coupling waveguides are $d_3 = 4.46$ mm, $d_4 = 4.27$ mm, and $\theta_2 = 45°$, $\theta_3 = 44.8°$, respectively. The vanishing of degeneracy can be explained by the broken primitive translation symmetry of $\mathcal{L}_x$.

Next, we investigate the projected band structures and the related characteristics of two-strip supercell models without and with the staggered dimerization couplings by using TBM and FWS. Figures 3(a) and 3(b) show the band structures for the strip model where all the coupling strengths are identical, with an open boundary condition in x direction but a periodic boundary condition in y direction. In Figs. 3(a) and 3(b), the black-color bands are featured with p_y orbital, which has a fourfold degenerate Dirac point protected by the projective translation symmetry and time-reversal symmetry. The other gray bands are featured with p_x orbital. Clearly, the results obtained by TBM agree with the ones from FWS. As the dimerization couplings are introduced along the x axis, the Dirac point is lifted as the primitive translation symmetry $\mathcal{L}_x$ is broken and a band gap emerges, which is shown in Fig. 3(c). In the band gap, two entangled and twisted edge bands (orange lines) are apparently observed, which are named by Edge_I modes. The Edge_I modes are p_y-orbital modes, which are detached from the bulk modes as shown in Fig. 3(c), which stands for a single band that forms a Möbius twist protected by both the translation symmetry $\mathcal{L}_y$ and sublattice symmetry $\mathcal{S}$. Besides the Edge_I modes, the emerged blue bands in the band gap are the edge states belonging to the other type, which are named by Edge_II modes and are yielded by the role of p_x orbital. In Fig. 3(d), the simulated projective band structures are in good agreement with the theoretical ones in Fig. 3(c). Note that there exists a weak shift of edge-state bands due to the presence of inevitable long-range and intermode couplings, which changes the symmetries of our acoustic model. In Fig. 3(d), the two Möbius edge-state bands

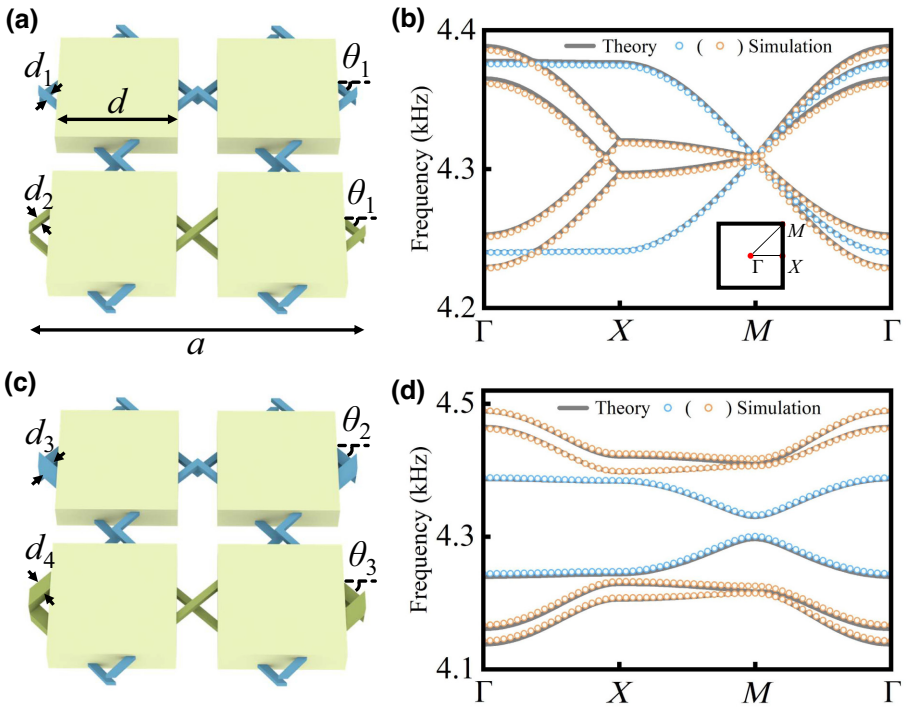

FIG. 2. The primitive-cell models and band structures. (a) A primitive cell with identical coupling strengths for the intracell and intercell hoppings. (b) The band structures of the model in (a). The circles are numerical simulation results (blue circles, p_y orbital modes; orange circles, p_x orbital modes), while the solid lines are obtained by the TBM. (c),(d) A primitive cell with coupling dimerization in x direction and the corresponding band structures.

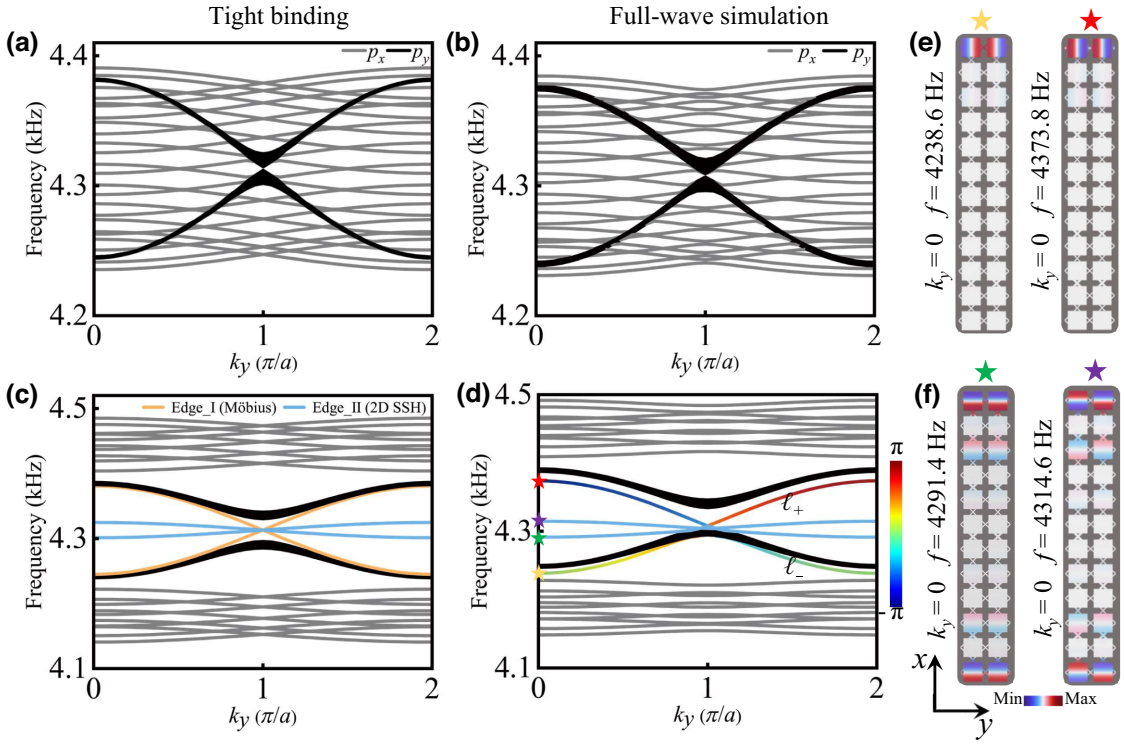

FIG. 3. The projected band structures and the Möbius edge states. (a),(b) Theoretical and simulated projected band structures for a strip supercell under the open boundary condition in x direction and the periodic boundary condition in y direction, where the coupling strengths are the same ($|t_1| = |t_2|$). The bands denoted by the black lines correspond to p_y-orbital modes featured with a fourfold Dirac degeneracy. The bands denoted by the gray lines are the p_x-orbital modes. (c),(d) Theoretical and simulated projected band structures for a supercell under the same boundary conditions in (a),(b), where the coupling strengths are different ($|t_1| < |t_2|$). In the band gap, the pair of twofold edge bands (the orange curves, Edge_I) features a Möbius twist, while the paired blue-color bands correspond to the edge modes (Edge_II) for the 2D SSH model. Here the color scale of Edge_I indicates the phase of eigenvalues $\ell\pm$ for the projective translation operator. (e),(f) The eigenfields for different frequencies at $k_y = 0$ for Edge_I and Edge_II, respectively, which are marked by the color-encoded stars in (d).

with opposite group velocities are separately locked to the two eigenvalues $\ell\pm$ of the translational operator $\mathcal{L}_y$, which features a 4π periodicity. The simulated eigenfield distributions of Edge_I (Möbius) and Edge_II (2D SSH) for the strip model with coupling dimerization are, respectively, displayed in Figs. 3(e) and 3(f), which illustrate obvious oriented p-orbital features.

Next, we implement simulations to analyze the responses and show the features of orbital-dependent Möbius TI. Figure 4(a) exhibits an as-constructed finite-size FWS model, which comprises 12×12 resonators. Owing to the orientations of p-orbital modes, specific types of sources are demanded to well excite the edge and bulk states. Here we utilize an orbital source formed by two out-of-phase sound signals to excite the Möbius edge modes and bulk modes, which are separately marked by the colored stars and circles in pairs as shown in Fig. 4(a). The captured response spectra at the edge (orange region) and in the bulk (black region) are shown in the left panel of Fig. 4(b). Evidently, there exist two peaks for the bulk modes, corresponding to the two separated black bands in Fig. 3(d). There also emerges one prominent peak for the edge modes, which corresponds to the Möbius-twisted band in the gap shown in Fig. 3(d).

By rotating the orbital sources in Fig. 4(a) by 90°, we will obtain another type of edge modes, viz., Edge_II modes, as the consequence of p_x-orbital excitation, as shown in the right panel of Fig. 4(b), where the edge and bulk spectra match well with the results in Fig. 3(d). We also present the pressure-field distributions for the Edge_I (Möbius) and the Edge_II (2D SSH) modes in Figs. 4(c) and 4(d), which feature the hallmarks of p orbitals.

We further show the variations under the situation where a supercell is periodical in the x direction but finite in the y direction in Fig. 5, in contrast to the case in Fig. 3. Figures 5(a) and 5(b), respectively, present the corresponding projective band structures via the TBM and FWS, matching well with each other. The blue and black curves are the bulk bands yielded by the p_y- and p_x-orbital modes, respectively. As expected, the two edge bands aroused by the p orbitals both vanish in the band gaps. To identify this, we show the transmission spectra in Figs. 5(c) and 5(d), where

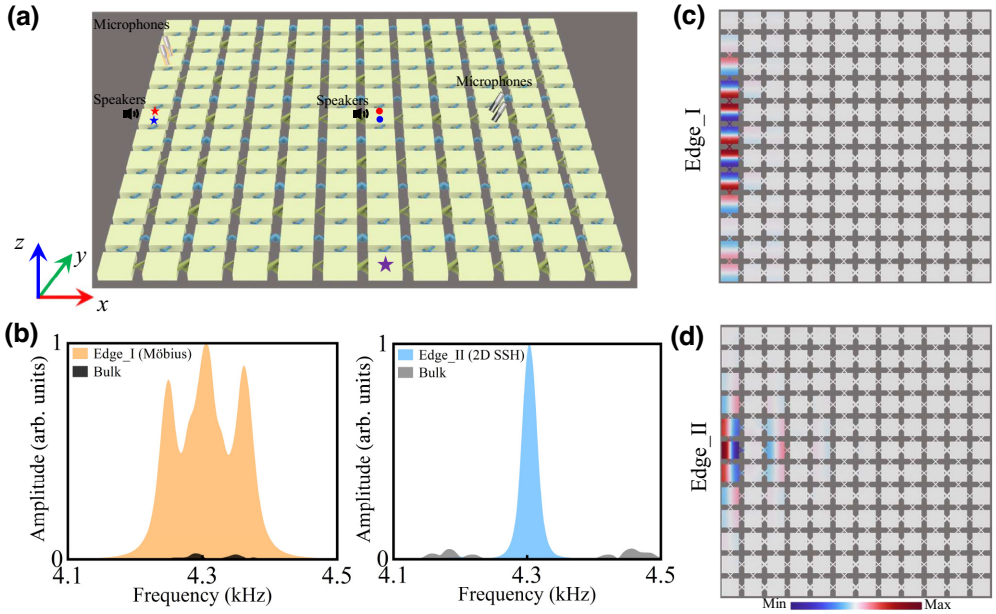

FIG. 4. Acoustic implementation of a 2D Möbius insulator. (a) A finite-size 12 × 12 model. In the resonators with the colored stars and circles marked in pairs, the out-of-phase speakers are located for exciting the edge and bulk modes. The paired microphones are utilized to detect the acoustic responses of the edge (bulk) modes. (b) The response spectra for the orbital-dependent edge states. Left: the excitation spectra for the Edge_I (Möbius) states and the corresponding bulk states with orbital sources marked in (a). Right: the excitation spectra for Edge_II (2D SSH) states and the associated bulk states. (c),(d) The pressure-field distributions for the Edge_I and Edge_II states, respectively.

the orbital sources are located at the resonator marked by the purple star at the bottom of the model in Fig. 4(a), with the orbital-source orientation the same as the ones at the middle resonator. Obviously, in Fig. 5(c), there exist two peaks corresponding to the bulk bands, in accordance with the case of bulk spectrum in the left panel of Fig. 4(b). With

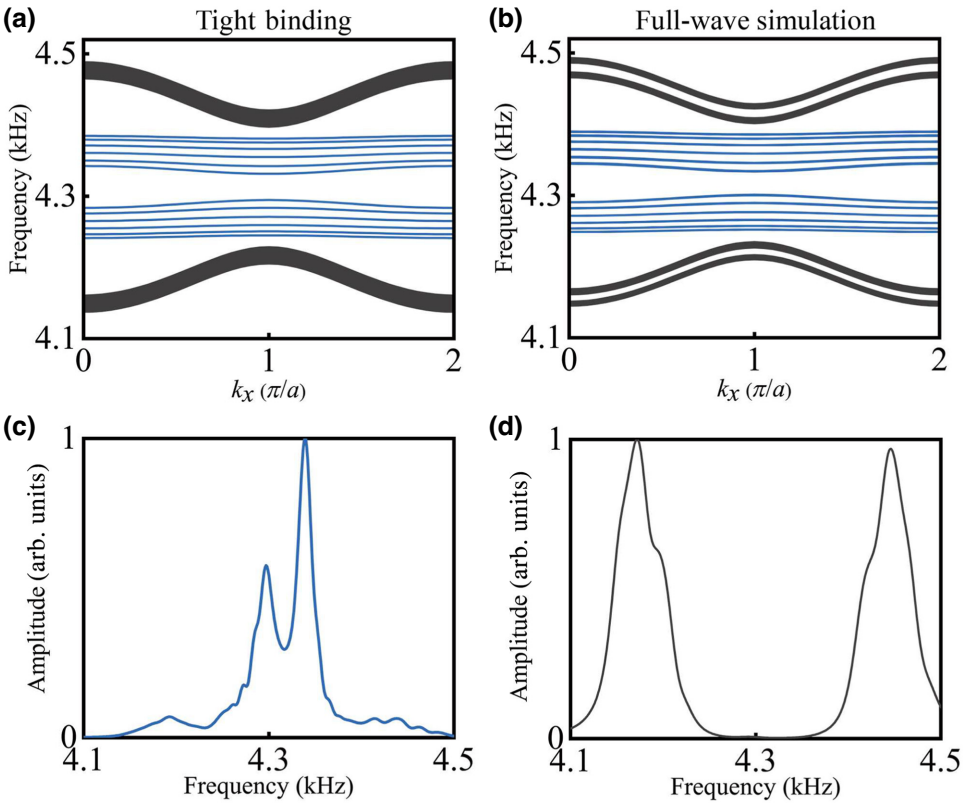

FIG. 5. (a),(b) Theoretical and simulated projective energy bands for the striped supercells under open boundary condition in the y direction but periodic boundary condition in the x direction, where $|t_1| < |t_2|$. The blue (black) lines represent the bulk bands for the p_y (p_x) orbital modes. (c),(d) The response spectra as the orbital sources are located in the resonators marked by the star at the bottom of the model in Fig. 4(a).

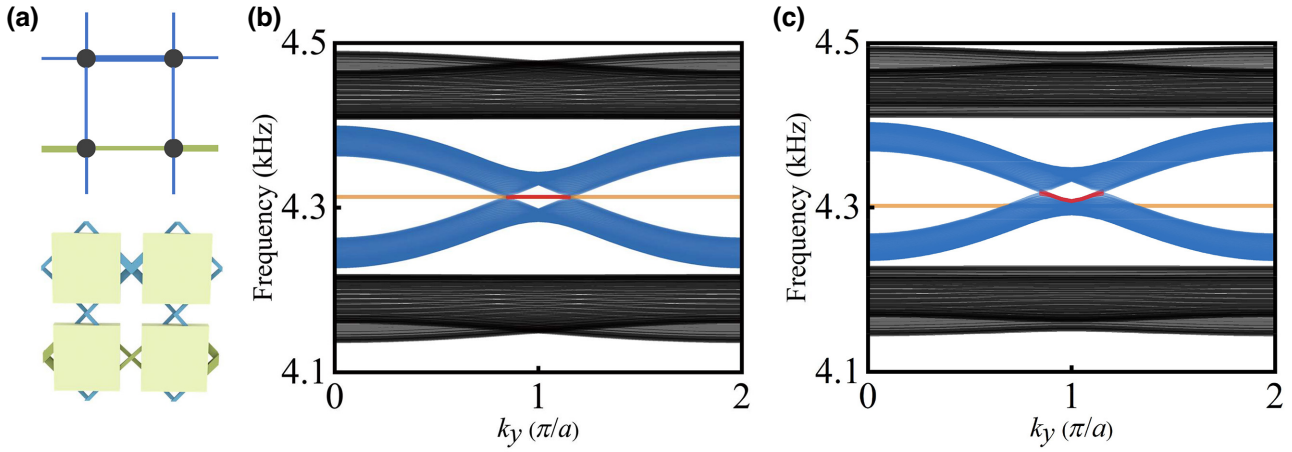

FIG. 6. Semimetal phase in the orbital acoustic lattice. (a) Schematics of a primitive cell. (b),(c) Projected energy bands obtained by TBM and FWS, respectively. The emerging edge modes (red lines) link the projections of Fermi points. The bulk bands from p_y orbitals are represented by blue curves. The flat bands (orange lines) in the band gap and the black bulk bands are the results from p_x orbital.

the orbital sources rotated by 90°, two separated peaks emerge in the spectrum as shown in Fig. 5(d), matching well with the scenario of the bulk spectrum in the right panel of Fig. 4(b).

IV. ORBITAL SEMIMETAL PHASE

In this section, we illustrate an orbital semimetal phase by an alternative dimerization coupling in the acoustic square lattice. Figure 6(a) shows the schematic diagram (top) and the realistic acoustic cavity-tube model (bottom) of the primitive cell. The structural parameters of the cavity and coupling tubes are the same with the ones used in Fig. 2(c). Using TBM, we calculate the projective dispersions via a supercell when the boundary condition in the y direction is periodical and in the x direction is open, which is displayed in Fig. 6(b). Clearly, the edge bands denoted by the red lines that connect the projections of Fermi points are directly visualized. The emerged orange flat bands as well as the black bulk bands arise from the p_x orbital. In contrast, we carry out FWS on an acoustic supercell model. The simulated result is presented in Fig. 6(c), which reproduces well the theoretical result in Fig. 6(b). The shifts of edge bands and flat bands in Fig. 6(c) occur due to the presence of inevitable long-range and intermode couplings that weakly impact the symmetries of the acoustic model.

V. CONCLUSIONS

In summary, we have investigated the orbital-dependent gauge fields in acoustic lattices. We find that by means of acoustic cavities that support degenerate p orbitals and manipulation of the related orbital couplings, we can readily realize the 2D SSH model with zero flux and the Möbius topological insulator with synthetic π flux per plaquette under different orbital excitations. The hybrid SSH edge modes and Möbius edge modes induced by different orbitals are unambiguously visualized by TBM and FWS. The orbital-dependent Möbius topological insulator is demonstrated by frequency responses and excitation field distributions, where the orbital sources are utilized. Furthermore, we identify the orbital-selective semimetal phase as well as the orbital-dependent flat band in the bulk bands of the acoustic square lattice. The essential interplay between acoustic degenerate (or hybrid) orbitals and synthetic gauge fields opens a door for the exploration of orbital-related topological physics and shows potentials for the acoustic applications, such as trapping and sensing.

ACKNOWLEDGMENTS

This work was supported by the National Natural Science Foundation of China through Grant No. 12304492.

APPENDIX A: ROBUSTNESS OF THE MÖBIUS EDGE STATES

Here we show that the Möbius edge states are robust against perturbations. To identify this, we utilize a supercell that is periodical in y direction and finite in x direction and introduce perturbations on the couplings and on-site eigenfrequencies. With the theory and analyses discussed above, the projective translational symmetry $\mathcal{L}_y$ and the sublattice symmetry $\mathcal{S}$ synergistically protect the Möbius edge states. We first display the scenario where both $\mathcal{L}_y$ and $\mathcal{S}$ are preserved. Specifically, we introduce variations to the intra- and intercell couplings in y direction at the edge, for which the calculated dispersions are shown in Fig. 7(a). The topological edge bands are very stable in the band gap and manifest the Möbius characteristics. However, when we break $\mathcal{L}_y$ by only adding intracell coupling, a gap will emerge in the Möbius edge bands, as displayed

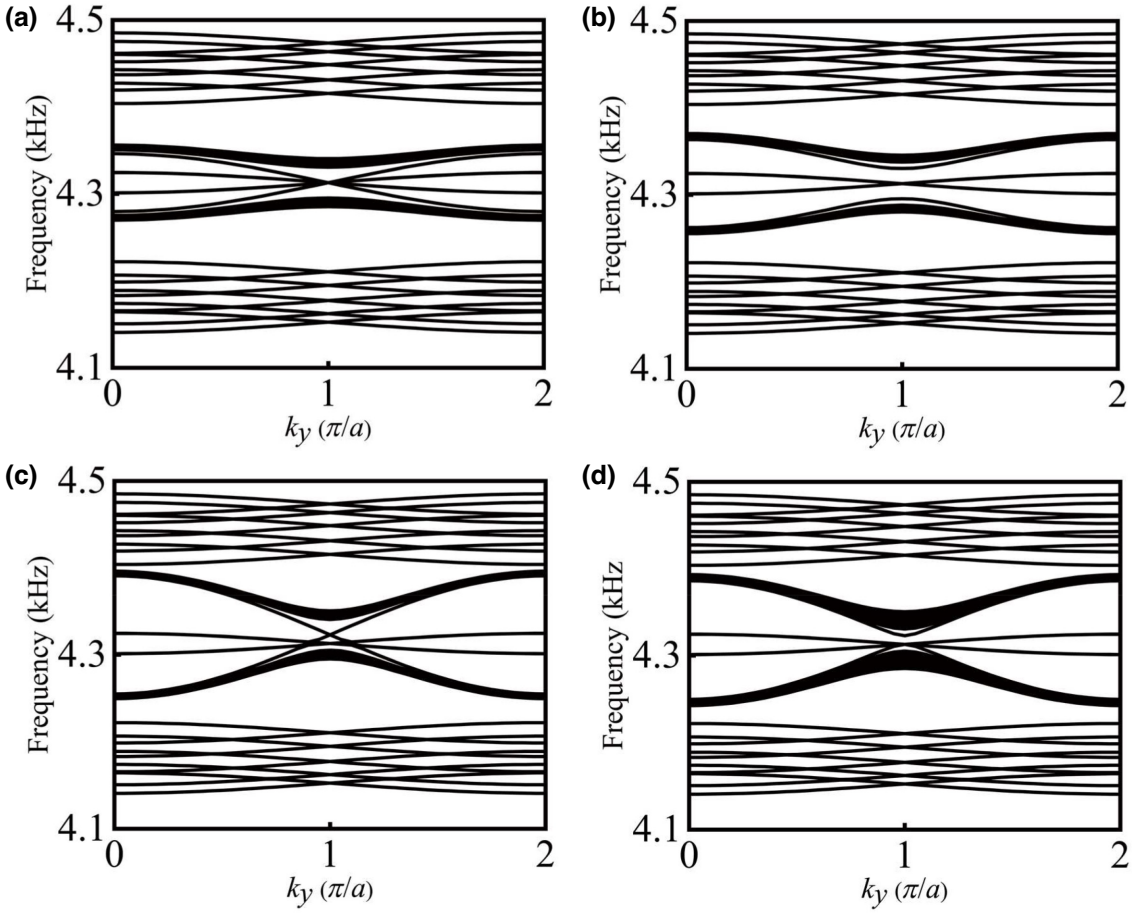

FIG. 7. Robustness of the Möbius edge states. The band structures under the variations of the projective translational symmetry $\mathcal{L}_y$ and the sublattice symmetry $\mathcal{S}$. (a) The case when both $\mathcal{L}_y$ and $\mathcal{S}$ are preserved. (b) The case when $\mathcal{L}_y$ is broken and $\mathcal{S}$ is preserved. (c) The case when $\mathcal{L}_y$ is preserved and $\mathcal{S}$ is broken. (d) The case when both $\mathcal{L}_y$ and $\mathcal{S}$ are broken.

in Fig. 7(b). Moreover, in the scenario where $\mathcal{L}_y$ is preserved but $\mathcal{S}$ is broken by adding some perturbations to the on-site energy (or eigenfrequencies), the Möbius edge bands are shifted, as illustrated in Fig. 7(c). When both $\mathcal{L}_y$ and $\mathcal{S}$ are broken, a gap will emerge in the shifted Möbius edge bands, as shown in Fig. 7(d). Thus, from the results in Fig. 7, we find that the Möbius edge states are very robust against the perturbations with both $\mathcal{L}_y$ and $\mathcal{S}$ preserved.

APPENDIX B: A PROPOSAL FOR THE EXPERIMENTAL REALIZATION

The finite-size resonator sample can be fabricated by the three-dimensional (3D) printing technique, which has been widely utilized in the realization of acoustic topological insulators [4,15,21]. To facilitate the sound excitation and detection, four small holes can be perforated on the top of each disk-shaped resonator according to the polarization of the degenerate orthogonal orbitals, and the holes should be sealed when not in use. For the generation of orbital sound, a pair of speakers connected with the signal generator are set as the out-of-phase source at the positions marked by the color-coded stars (circles) in Fig. 4(a). For the detection, we can utilize a microphone to measure both the amplitude and phase responses, with the other one in the same resonator as phase reference, which are shown by the sketched microphones in Fig. 4(a). The captured sound signals, which are recorded and processed by a network analyzer, can be furtherly utilized to map out the response spectra as well as the pressure-field distributions.

[1] K. Fang, Z. Yu, and S. Fan, Photonic Aharonov-Bohm effect based on dynamic modulation, Phys. Rev. Lett. **108**, 153901 (2012).

[2] K. Fang, Z. Yu, and S. Fan, Realizing effective magnetic field for photons by controlling the phase of dynamic modulation, Nat. Photonics **6**, 782 (2012).

[3] M. Kremer, I. Petrides, E. Meyer, M. Heinrich, O. Zilberberg, and A. Szameit, A square-root topological insulator with non-quantized indices realized with photonic Aharonov-Bohm cages, Nat. Commun. **11**, 907 (2020).

[4] Y. Meng, S. Lin, B.-j. Shi, B. Wei, L. Yang, B. Yan, Z. Zhu, X. Xi, Y. Wang, Y. Ge, S.-q. Yuan, J. Chen, G.-G. Liu, H.-x. Sun, H. Chen, Y. Yang, and Z. Gao, Spinful topological phases in acoustic crystals with projective PT symmetry, Phys. Rev. Lett. **130**, 026101 (2023).

[5] Q. Lin and S. Fan, Light guiding by effective gauge field for photons, Phys. Rev. X **4**, 031031 (2014).

[6] Y. Lumer, M. A. Bandres, M. Heinrich, L. J. Maczewsky, H. Herzig-Sheinfux, A. Szameit, and M. Segev, Light guiding by artificial gauge fields, Nat. Photonics **13**, 339 (2019).

[7] Y. Yang, Y. Ge, R. Li, X. Lin, D. Jia, Y.-j. Guan, S.-q. Yuan, H.-x. Sun, Y. Chong, and B. Zhang, Demonstration of negative refraction induced by synthetic gauge fields, Sci. Adv. **7**, eabj2062 (2021).

[8] C. Qin, F. Zhou, Y. Peng, D. Sounas, X. Zhu, B. Wang, J. Dong, X. Zhang, A. Alù, and P. Lu, Spectrum control through discrete frequency diffraction in the presence of photonic gauge potentials, Phys. Rev. Lett. **120**, 133901 (2018).

[9] W. Song, T. Li, S. Wu, Z. Wang, C. Chen, Y. Chen, C. Huang, K. Qiu, S. Zhu, Y. Zou, and T. Li, Dispersionless coupling among optical waveguides by artificial gauge field, Phys. Rev. Lett. **129**, 053901 (2022).

[10] A. Celi, P. Massignan, J. Ruseckas, N. Goldman, I. B. Spielman, G. Juzeliunas, and M. Lewenstein, Synthetic gauge fields in synthetic dimensions, Phys. Rev. Lett. **112**, 043001 (2014).

[11] L. Yuan, Y. Shi, and S. Fan, Photonic gauge potential in a system with a synthetic frequency dimension, Opt. Lett. **41**, 741 (2016).

[12] L. Yuan, Q. Lin, A. Zhang, M. Xiao, X. Chen, and S. Fan, Photonic gauge potential in one cavity with synthetic frequency and orbital angular momentum dimensions, Phys. Rev. Lett. **122**, 083903 (2019).

[13] R. Fleury, A. B. Khanikaev, and A. Alu, Floquet topological insulators for sound, Nat. Commun. **7**, 11744 (2016).

[14] M. Serra-Garcia, V. Peri, R. Susstrunk, O. R. Bilal, T. Larsen, L. G. Villanueva, and S. D. Huber, Observation of a phononic quadrupole topological insulator, Nature **555**, 342 (2018).

[15] Y. Qi, C. Qiu, M. Xiao, H. He, M. Ke, and Z. Liu, Acoustic realization of quadrupole topological insulators, Phys. Rev. Lett. **124**, 206601 (2020).

[16] C. Jörg, G. Queraltó, M. Kremer, G. Pelegrí, J. Schulz, A. Szameit, G. von Freymann, J. Mompart, and V. Ahufinger, Artificial gauge field switching using orbital angular momentum modes in optical waveguides, Light: Sci. Appl. **9**, 150 (2020).

[17] G. Caceres-Aravena, D. Guzman-Silva, I. Salinas, and R. A. Vicencio, Controlled transport based on multiorbital Aharonov-Bohm photonic caging, Phys. Rev. Lett. **128**, 256602 (2022).

[18] Y. X. Zhao, Y.-X. Huang, and S. A. Yang, Z2-projective translational symmetry protected topological phases, Phys. Rev. B **102**, 161117 (2020).

[19] Y. X. Zhao, C. Chen, X.-L. Sheng, and S. A. Yang, Switching spinless and spinful topological phases with projective PT symmetry, Phys. Rev. Lett. **126**, 196402 (2021).

[20] L. B. Shao, Q. Liu, R. Xiao, S. A. Yang, and Y. X. Zhao, Gauge-field extended $k\cdot p$ method and novel topological phases, Phys. Rev. Lett. **127**, 076401 (2021).

[21] H. Xue, Z. Wang, Y.-X. Huang, Z. Cheng, L. Yu, Y. X. Foo, Y. X. Zhao, S. A. Yang, and B. Zhang, Projectively enriched symmetry and topology in acoustic crystals, Phys. Rev. Lett. **128**, 116802 (2022).

[22] H. Xue, Z. Y. Chen, Z. Cheng, J. X. Dai, Y. Long, Y. X. Zhao, and B. Zhang, Stiefel-Whitney topological charges in a three-dimensional acoustic nodal-line crystal, Nat. Commun. **14**, 4563 (2023).

[23] Z. Y. Chen, S. A. Yang, and Y. X. Zhao, Brillouin Klein bottle from artificial gauge fields, Nat. Commun. **13**, 2215 (2022).

[24] T. Li, J. Du, Q. Zhang, Y. Li, X. Fan, F. Zhang, and C. Qiu, Acoustic Möbius insulators from projective symmetry, Phys. Rev. Lett. **128**, 116803 (2022).

[25] Y. Tokura and N. Nagaosa, Orbital physics in transition-metal oxides, Science **288**, 462 (2000).

[26] M. Imada, A. Fujimori, and Y. Tokura, Metal-insulator transitions and correlated metals in d-electron systems, Rev. Mod. Phys. **70**, 1039 (1998).

[27] G. Wirth, M. Ölschläger, and A. Hemmerich, Evidence for orbital superfluidity in the P-band of a bipartite optical square lattice, Nat. Phys. **7**, 147 (2010).

[28] K. Sun, W. V. Liu, A. Hemmerich, and S. Das Sarma, Topological semimetal in a fermionic optical lattice, Nat. Phys. **8**, 67 (2011).

[29] A. P. Slobozhanyuk, A. N. Poddubny, A. E. Miroshnichenko, P. A. Belov, and Y. S. Kivshar, Subwavelength topological edge states in optically resonant dielectric structures, Phys. Rev. Lett. **114**, 123901 (2015).

[30] P. St-Jean, V. Goblot, E. Galopin, A. Lemaître, T. Ozawa, L. Le Gratiet, I. Sagnes, J. Bloch, and A. Amo, Lasing in topological edge states of a one-dimensional lattice, Nat. Photonics **11**, 651 (2017).

[31] M. R. Slot, S. N. Kempkes, E. J. Knol, W. M. J. van Weerdenburg, J. J. van den Broeke, D. Wegner, D. Vanmaekelbergh, A. A. Khajetoorians, C. Morais Smith, and I. Swart, p-band engineering in artificial electronic lattices, Phys. Rev. X **9**, 011009 (2019).

[32] T. S. Gardenier, J. J. van den Broeke, J. R. Moes, I. Swart, C. Delerue, M. R. Slot, C. M. Smith, and D. Vanmaekelbergh, p orbital flat band and Dirac cone in the electronic honeycomb lattice, ACS Nano **14**, 13638 (2020).

[33] J. Schulz, J. Noh, W. A. Benalcazar, G. Bahl, and G. von Freymann, Photonic quadrupole topological insulator using orbital-induced synthetic flux, Nat. Commun. **13**, 6597 (2022).

[34] Z. Liu, G. Wei, H. Wu, and J.-J. Xiao, Möbius edge band and Weyl-like semimetal flat-band in topological photonic waveguide array by synthetic gauge flux, Nanophotonics **12**, 3481 (2023).

[35] C. Jiang, Y. Song, X. Li, P. Lu, and S. Ke, Photonic Möbius topological insulator from projective symmetry in multiorbital waveguides, Opt. Lett. **48**, 2337 (2023).

Correction: The previously published Figure 1(b) was converted improperly during the production cycle and is now rendered optimally.